Science

Experimental observation of high thermal conductivity in boron arsenide

Joon Sang Kang, Man Li, Huan Wu, Huuduy Nguyen and Yongjie Hu

submitted 12 March 2018; accepted 21 June 2018
published online July 5, 2018

Science (print ISSN 0036-8075; online ISSN 1095-9203) is published by the American Association for the Advancement of Science, 1200 New York Avenue NW, Washington, DC 20005.

REPORT

THERMAL CONDUCTIVITY

Experimental observation of high thermal conductivity in boron arsenide

Joon Sang Kang, Man Li, Huan Wu, Huuduy Nguyen, Yongjie Hu*

Improving the thermal management of small-scale devices requires developing materials with high thermal conductivities. The semiconductor boron arsenide (BAs) is an attractive target because of ab initio calculation indicating that single crystals have an ultrahigh thermal conductivity. We synthesized BAs single crystals without detectable defects and measured a room-temperature thermal conductivity of 1300 watts per meter-kelvin. Our spectroscopy study, in conjunction with atomistic theory, reveals that the distinctive band structure of BAs allows for very long phonon mean free paths and strong high-order anharmonicity through the four-phonon process. The single-crystal BAs has better thermal conductivity than other metals and semiconductors. Our study establishes BAs as a benchmark material for thermal management applications and exemplifies the power of combining experiments and ab initio theory in new materials discovery.

The decreasing size of modern electronics makes heat dissipation one of the most critical technological challenges. The worldwide semiconductor industry, which has powered the information technology revolution since the 1960s, acknowledged in 2016 that Moore's law is nearing its end (*1*). A major issue is the enormous amount of waste heat generated during electronic device operation (*2*, *3*). For example, a U.S. data center devotes about 50% of its total electricity use to cooling (*4*). At the nanoscale, the power density of hot spots in current transistors is approaching that of the Sun's surface (*5*). Low thermal conductivity and heat dissipation rates severely degrade the performance and energy efficiency of electronic and photonic devices. Thermal management is arguably the biggest roadblock for next-generation devices, such as microprocessors and integrated circuits, light-emitting diodes, and high-power radio frequency devices, to name just a few (*1*, *5*).

Discovering high thermal conductivity (HTC) materials is needed to enable efficient heat dissipation from hot spots and improve device performance. So far, much of the research has been focused on carbon-based crystals—diamond, graphene, and carbon nanotubes. Although these materials can have exceptional heat transfer properties, there are several drawbacks for widespread use. Diamond, the most developed material for passive cooling of high-power electronics, suffers from high cost, slow synthesis rates, low quality, and challenging integration with semiconductors. Degradation of thermal conductivity plagues graphene and nanotubes when assembled into practical sizes, owing to ambient interactions and disorder scattering. Their intrinsic anisotropy creates other challenges for applications.

Fundamentally, understanding the origins of HTC remains a challenge. The conventionally accepted criteria for HTC materials are (i) small average atomic mass ($\bar{M}$); (ii) strong interatomic bonding; (iii) simple crystal structure; and (iv) low anharmonicity (*6*–*8*). Criteria (i) and (ii) imply a large Debye temperature (Θ_D) and provide the commonly used rule of thumb that thermal conductivity increases with decreasing $\bar{M}$ and increasing Θ_D. Diamond is the prototypical crystal. Diamond's two-atom primitive unit cell, light carbon mass, and stiff covalent bonding result in an exceptionally high value for thermal conductivity. Recent ab initio calculations show excellent agreement with the measured thermal conductivity of a wide range of materials (*8*–*16*), including silicon, diamond, graphene, and carbon nanotubes. Such calculations provide new physical insights into the nature of phonon thermal transport and the HTC mechanism.

Recent ab initio theoretical work indicates that the conventional criteria for HTC materials are incomplete and points to new ones stemming from fundamental vibrational properties that can lead to HTC (*8*, *16*–*18*). These new criteria applied to binary compounds are (i) a large mass ratio of constituent atoms; (ii) bunching together of the acoustic phonon branches; and (iii) an isotopically pure heavy atom. The large mass ratio provides a large frequency gap between acoustic and optical phonons (a-o gap). According to materials examined thus far, bunching of the acoustic phonon dispersions tends to occur in crystals with light constituent atoms, such as boron and carbon, where it derives from an unusual interatomic bonding that lacks core p electrons (*19*). Criteria (i) and (ii) contribute to unusually weak phonon-phonon scattering (*20*) and a large intrinsic thermal conductivity, whereas criteria (i) and (iii) cause relatively weak scattering of phonons by isotopes (*21*, *22*). The ab initio theory identified the III-V zinc-blende compound, defect-free boron arsenide (BAs), as having an exceptionally high thermal conductivity of more than 1000 W/m·K (*8*, *16*–*18*). This predicted HTC exceeds that of most state-of-the-art HTC materials and more than triples that of the current industrial HTC standard, i.e., silicon carbide. BAs possesses an advantageous combination of properties that incorporates both conventional (light boron mass and stiff, almost pure, covalent bonding) and new criteria [large arsenic-to-boron mass ratio, bunching together of its acoustic phonon branches, and isotopically pure As (heavy) atom] (*8*, *16*–*18*).

Experimental efforts to synthesize and characterize BAs have been scarce (*17*). Although the growth of cubic BAs was reported in the 1950s, its detailed structural characterization and properties were not reported (*23*–*28*). Generally, boron-related materials are notably difficult to obtain in dense bulk form (*29*). The synthesis of BAs is further complicated by the high volatility of arsenic and the introduced vacancy defects, as well as the possible formation of subphases (e.g., $B_{12}As_2$). In a collaborative effort, we reported the earliest thermal measurements on cubic BAs using the time-domain thermoreflectance technique (*30*). Our thermal conductivity value of 190 W/m·K measured in BAs samples with a high density of defects is far below the theoretical expectation. Later study made improvement, but the samples still show defects and grain boundaries that degraded the crystal quality and thermal properties (*31*). On the basis of subsequent analysis and calculation, defect scattering plays a dominant role in those samples, which makes probing the actual intrinsic thermal conductivity of BAs impossible in the absence of high-quality BAs crystals (*32*).

Here, we synthesized high-quality single-crystal BAs and measured an ultrahigh thermal conductivity of 1300 W/m·K in our BAs crystals. This value exceeds that of most HTC materials and is consistent with the ab initio prediction (*8*, *16*–*18*). We characterized our samples with scanning electron microscopy, Raman spectroscopy, powder x-ray diffraction (P-XRD), single-crystal x-ray diffraction (S-XRD), and high-resolution transmission electron microscopy (HRTEM). BAs has a zinc-blende face-centered cubic (fcc) crystal structure in the $F\bar{4}3m$ space group, where boron and arsenic atoms are interpenetrating and covalently bonded to form a tetrahedral geometry (Fig. 1A). The Raman spectroscopy data (Fig. 1C) clearly show two peaks, at 700 and 720 cm^{-1}, corresponding to the separate vibrational behaviors of two boron isotopes (^{10}B and ^{11}B) in their natural abundance, respectively. The P-XRD peaks that we observed (Fig. 1D) are in agreement with the zinc-blende fcc crystal structure. Our S-XRD confirmed the $F\bar{4}3m$ space group and the crystal quality, and was performed to unambiguously verify the single domain, single-crystalline

School of Engineering and Applied Science, University of California, Los Angeles (UCLA), Los Angeles, CA 90095, USA.
*Corresponding author. Email: yhu@seas.ucla.edu

nature over entire crystals (*33*). Each of the reflections in the x-ray diffraction pattern (Fig. 1E) appears clearly as a single dot without distortion, indicating that the sample has no grain boundaries. To collect a complete dataset of all reciprocal lattice points through the whole crystal, we rotated BAs samples over 360° under x-ray excitation and collected diffraction data at every 0.3° rotation. The reconstructed reciprocal lattice images from the S-XRD [see [100] plane in Fig. 1F and (*34*)] confirms the single-domain, single-crystalline zinc-blende fcc structure with a cubic lattice constant of 4.78 Å over the entire BAs sample. We used a focused ion beam to thin samples to ~100 nm for HRTEM (Fig. 1G). HRTEM images (Fig. 1H) clearly demonstrate the atomically resolved single-crystal lattice of our BAs sample. The reciprocal lattice peaks obtained from two-dimensional Fourier transforms of the lattice-resolved image (inset to Fig. 1H) were indexed in the zinc-blende structure with the zone axes along the [111] direction. The measured distance between each fringe is 1.69 Å, which is consistent with $(\bar{2}02)$ lattice spacing of BAs crystals (*23*) given the diffraction selection rules (*35*).

We characterized the thermal properties and phonon transport using ultrafast optical pump-probe spectroscopy based on the time-domain thermoreflectance (TDTR) technique (*15*, *30*, *36*). TDTR is well suited for the study as no physical contact is required with the sample and the measurement can provide high spatial resolution at the micrometer scale. We exposed our sample to a train of short pulses from a pump laser that creates a temperature rise at the sample surface (Fig. 2A). The transient temperature decay, caused by the heat impulse, was monitored with another probe pulse that is delayed in time with respect to the pump using a mechanical delay stage. The thermal conductivity was obtained by fitting the full transient decay curve, acquired by varying the time delay, to a thermal model (Fig. 2B). We measured a room-temperature thermal conductivity of our high-quality BAs crystals of ~1300 W/m·K. This value exceeds that of any known metal and semiconductor and is more than three times as high as that of industrial standards (copper and silicon carbide).

We simultaneously performed TDTR measurements on single-crystal BAs, diamond, and cubic boron nitride (BN) samples to ensure accuracy and provide direct comparison between the materials (*34*). We measured the temperature-dependent thermal conductivity of these samples from 300 to 600 K (Fig. 2C). Our thermal conductivity values for diamond (from 2200 to 1050 W/m·K for the temperature range) are consistent with values from the literature (*37*–*39*) and validate our approach. All samples had decreased thermal conductivities with increased temperature, indicating Umklapp scattering due to increasing phonon population. This also indicates a high single-crystal quality as phonon-defect scattering behavior is not observed. The thermal conductivity of BAs is almost twice that of cubic BN, making BAs the second-highest thermally conducting material among all known isotropic materials, exceeded only by diamond. As a semiconductor, BAs has a high potential for manufacturing integration and holds promise for thermal management applications.

Fundamentally, thermal transport in solids can be described by the interactions of phonons, i.e., the quantum-mechanical modes of lattice vibrations (*6*). Thermal conductivity results from phonon scattering processes that are closely related to the structure of materials. Phonon scattering usually includes Umklapp phonon-phonon scattering (τ_U), phonon-electron scattering ($\tau_{ph\text{-}e}$), mass fluctuation scattering (τ_M), and boundary scattering (τ_B) that can be characterized by the following relaxation rate $1/\tau$ (τ is the corresponding relaxation time):

$$\frac{1}{\tau} = \frac{1}{\tau_U} + \frac{1}{\tau_{ph\text{-}e}} + \frac{1}{\tau_M} + \frac{1}{\tau_B} \quad (1)$$

Previous research indicates that the last two terms of this equation—τ_M and τ_B—play important roles in the thermal conductivity of crystals with defects and grain boundaries (*32*). $\tau_{ph\text{-}e}$ is non-negligible for doped semiconductors, or metals with sufficiently high electron density. Notably, the first term of the equation—τ_U—describes the thermal conductivity of perfect single crystals without any defects, and therefore is expected to be the dominant transport mechanism in our high-quality BAs single crystals. However, a persistent fundamental question regarding the high-order phonon anharmonicity, in particular for BAs, remains in the field of atomistic phonon theory. For many decades, thermal transport in solids

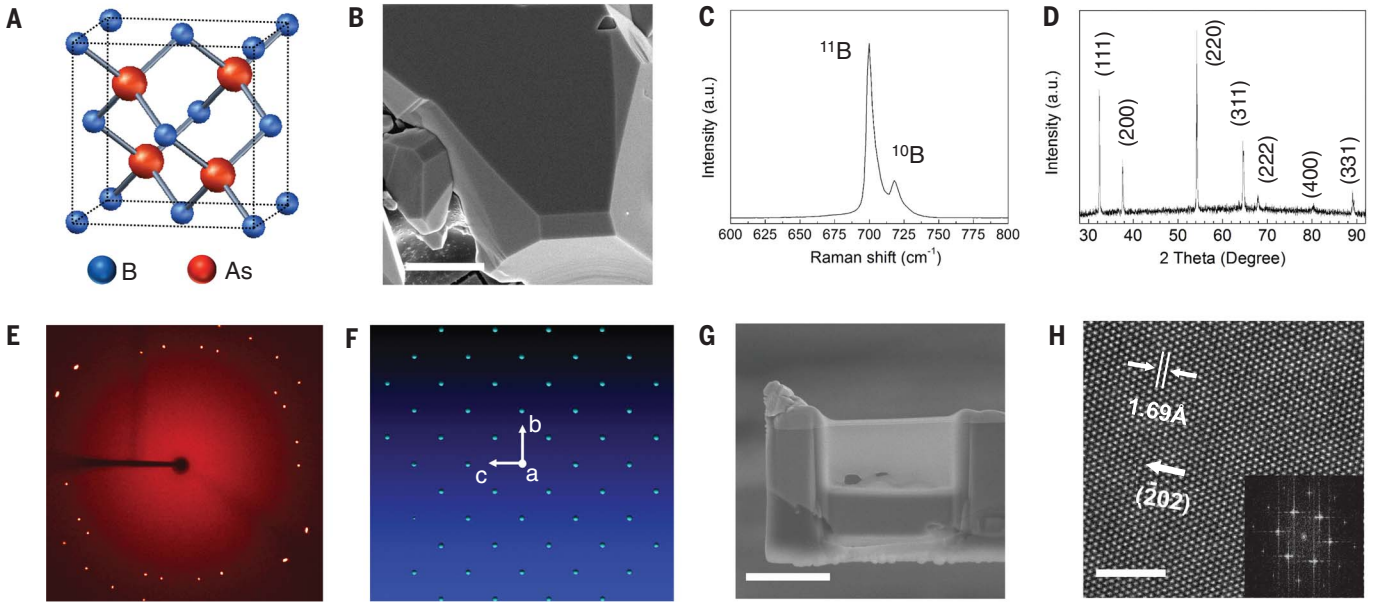

Fig. 1. Structural characterizations of single-crystal BAs. (**A**) Schematic of the zinc-blende crystal structure of cubic BAs, resembling that of diamond. (**B**) Scanning electron microscope (SEM) image of BAs. Scale bar: 5 μm. (**C**) Raman spectra of BAs crystals. (**D**) Powder x-ray diffraction measurements. (**E**) Single-crystal x-ray diffraction image of BAs. (**F**) Constructed reciprocal lattice of BAs from the complete dataset of single-crystal x-ray diffraction measurements, representing a clear single-crystal reciprocal space over the entire crystal. The lattice constant was measured as 4.78 Å for cubic BAs. (**G**) SEM image of a BAs sample thin slice (~100 nm) prepared by focused ion beam for HRTEM studies. Scale bar: 3 μm. (**H**) HRTEM image of BAs showing atomically resolved lattices. Inset: Two-dimensional Fourier transforms of the image depicting the [111] zone axes of BAs; the arrow indicates the crystal direction of $(\bar{2}02)$. Scale bar: 2 nm.

was considered to be governed by the three-phonon scattering process (*6*, *40*), and the effects of four-phonon and higher-order scattering processes were believed to be negligible. The three-phonon scattering was deployed in the initial ab initio calculations of the BAs thermal conductivity (*8*), but according to recent theory (*16*, *41*), the four-phonon scattering is important in certain materials such as BAs. The two density functional theory (DFT)–based calculations predict different thermal conductivity values for BAs. We compared our experimental measurements at different temperatures with two DFT theory predictions (Fig. 2D). In addition, to compare and exclude the effect of point defects, we performed three-phonon DFT calculation with vacancies (*34*) and included it in the figure. We found that our experimental results are in good agreement with the four-phonon DFT calculation, verifying that the Umklapp phonon scattering dominates phonon interactions. Moreover, our experiments indicate that, unlike in most materials, the probability of higher-order phonon scattering in BAs is important and cannot be ignored even around room temperature. The high-order anharmoniciy that we observed for BAs is due to its distinctive band structure (i.e., large a-o gap and large mass ratio) that leads to a relatively weak three-phonon process and provides sufficient numbers of possible four-phonon scattering configurations.

Another important phonon mechanism for HTC in BAs is the unique phonon mean free path (MFP) spectra that come from its extraordinary phonon band structure. MFPs represent the characteristic lengths corresponding to the distance over which heat carriers transmit thermal energy before being scattered; in general, MFPs can span several orders of magnitude—usually from ~1 nm to ~100 μm. According to the ab initio theory, BAs has a large phononic band gap between acoustic and optical phonon branches, which minimizes acoustic-optical phonon scattering and leads to MFPs longer than those of most common materials. In particular, BAs phonons with MFPs longer than 1 μm contribute to more than 90% of its total thermal conductivity (*18*). By comparison, for diamond and cubic BN, phonons with MFPs longer than 1 μm only contribute to about 30% of their total thermal conductivity. To gain further insight and verify the phonon MFP distribution in BAs, we probed the phonon spectral contribution by exploiting the size-dependent ballistic transport (*15*). In essence, thermal conductivity represents the spectral contribution from many different phonon modes and can be quantified using the cumulative thermal conductivity (*42*) expressed as

$$\kappa(\Lambda_m) = -\int_0^{\Lambda_M} \frac{1}{3} C \cdot v \cdot \Lambda \left(\frac{d\Lambda}{d\omega}\right)^{-1} d\Lambda \quad (2)$$

where C, v, and Λ are the phonon mode (ω)–dependent heat capacity, group velocity, and phonon MFP, respectively. The cumulative thermal conductivity—$\kappa(\Lambda_m)$—represents the contribution to the total thermal conductivity from all phonons with MFPs shorter than a certain value, Λ_m. This quantitative spectral information projects the contributions to thermal conductivity into characteristic length scales and is key to understanding thermal properties in connection with atomistic phonon theory (*42*).

Experimentally, this phonon MFP distribution information can be investigated by exploiting the ballistic (or nonequilibrium) heat conduction around a small heating area, with the physical concept described in our recently developed thermal spectral mapping spectroscopy technique (Fig. 3A) (*15*, *36*). In this measurement, hot phonons travel from the heated area into the underlying substrate material. The heat transfer regime is controlled by a characteristic thermal length, which is proportional to the heating size D, in comparison to phonon MFPs. In the diffusive limit, when $D >> \Lambda$, propagating phonons experience enough scattering to reach local thermal equilibrium. In this case, Fourier's law accurately describes the transport and heat flux, and the thermal conductivity of materials is simply the bulk value (κ_{bulk}). From the kinetic theory (*6*), the contribution to the total thermal conductivity from a specific phonon mode is $\kappa_{\omega,bulk} = \frac{1}{3} C_\omega \cdot v_\omega \cdot \Lambda_\omega$. As the heater size D decreases, phonons with $D < \Lambda$ will have fewer opportunities to scatter. In the ballistic limit ($D << \Lambda$), phonons propagate analogously to the thermal radiation over the whole region with a characteristic length of ~D. Therefore, the actual heat flux will deviate from the Fourier's law prediction for the quasi-ballistic, or ballistic, regimes (Fig. 3A). Mathematically, the actual heat flux is measured and fitted to Fourier's law to obtain an effective thermal conductivity (κ_{eff}), which gradually decreases in value for smaller Ds, as a higher portion of phonons evolves from diffusive to ballistic transport. The decrease in κ_{eff} (D) represents MFP spectra and should follow the same trend in $\kappa(\Lambda_m)$. Therefore, the size-dependent thermal conductivity measurement can provide a fundamental understanding of such MFP spectra, although the exact relationship between κ_{eff} and D requires careful atomistic and multiscale simulations and is a function of the heating geometry and materials (*15*, *36*).

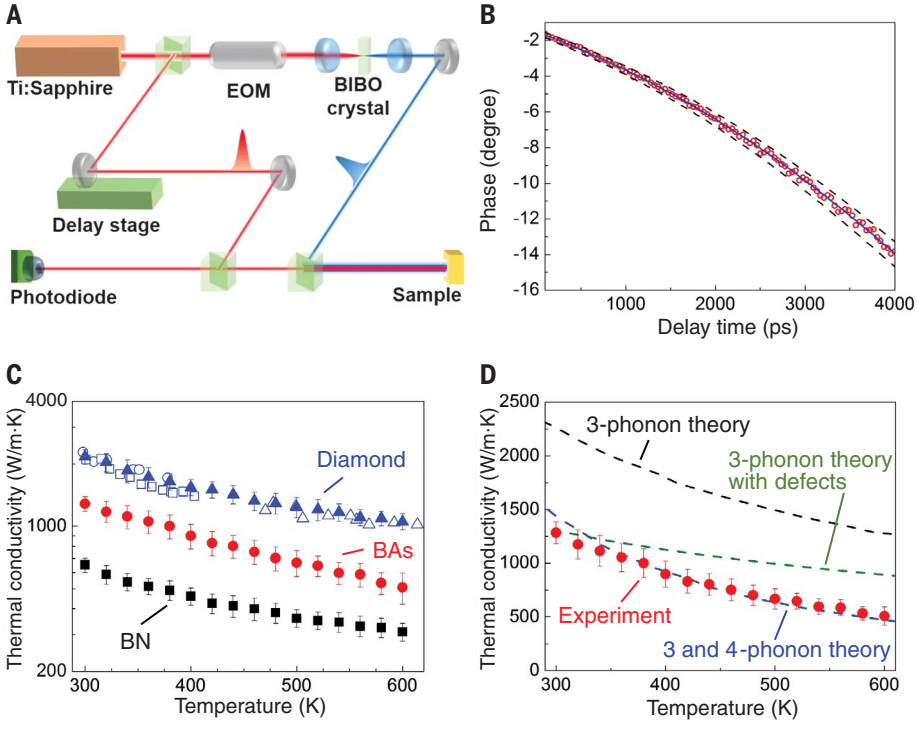

Fig. 2. Temperature-dependent thermal transport measurements. (**A**) Schematic of the setup for ultrafast pump-probe spectroscopy via the time-domain thermoreflectance (TDTR) technique. (**B**) Typical TDTR data: thermal reflectance phase signal versus time (red circles), fitted to the thermal transport model (blue line). Calculated curves (black dashed lines) with the thermal conductivity changed by ±10% of the best values to illustrate measurement accuracy. (**C**) Temperature-dependent (300 to 600 K) thermal conductivity of the three materials with the highest thermal conductivities: diamond, BAs, and boron nitride (BN). Black squares, red circles and blue triangles indicate cubic BN, BAs, and diamond, respectively. Also shown are literature data for diamond [open blue circles (*38*), squares (*37*), and triangles (*39*)]. (**D**) Experimentally measured thermal conductivity of BAs in comparison to ab initio predictions by DFT, considering the three-phonon scattering process (black dashed line) (*8*), the three- and four-phonon scattering process (blue dashed line) (*16*), and the three-phonon scattering process with point defects (green dashed line) (*34*).

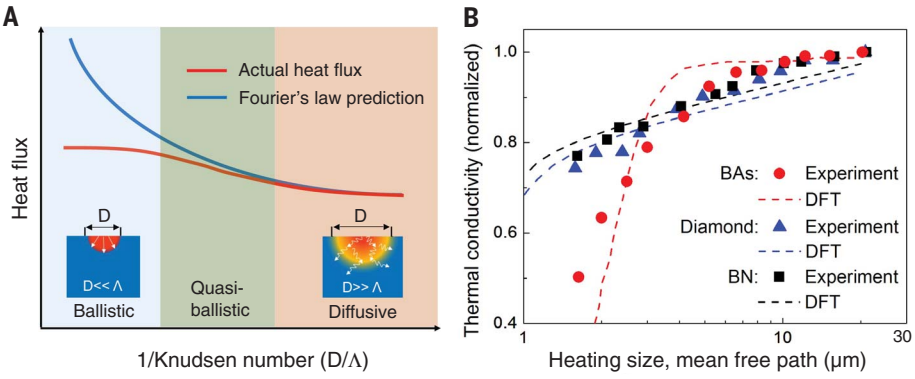

Fig. 3. Probing phonon mean free path spectra of BAs through size-dependent ballistic transport. (**A**) Schematic of heat flux for a fixed temperature difference as a function of the Knudsen number. Red and blue lines indicate the actual heat flux and the flux predicted by Fourier's law, respectively. Insets show that the thermal transport evolves from a diffusive to a ballistic regime when the heating size is gradually reduced. When the actual heat flux was measured and fitted to Fourier's law to obtain an effective thermal conductivity (κ_{eff}), a gradual reduction in κ_{eff} was expected with a decreasing heating size. Essentially, the κ_{eff} decrease is due to the evolution from diffusive to ballistic transport for the phonons with a mean free path comparable to the heating size, and thereby represents the phonon MFP spectra. (**B**) The normalized effective thermal conductivity was measured for the three best thermal conductors (BAs, diamond, and BN), as a function of heating diameters from 21 to 1.6 μm. Experimental results, compared with the MFP spectra calculated with DFT (*8*, *16*, *18*), indicate that in BAs, a large portion of phonons have long mean free paths, owing to the distinctive band structure of BAs.

In our experiments, the laser beam served as the heater, and we measured the effective thermal conductivity of materials by varying the laser heating size from 21 to 1.6 μm. The thermal conductivity of BAs, diamond, and cubic BN were measured simultaneously as a function of the heating sizes (Fig. 3B). The results clearly show that ballistic transport occurs in all three materials, but that their thermal conductivity decreases differ. For diamond and cubic BN, κ_{eff} decreases by ~26 and 23%, respectively, when reducing the laser heating size from 21 to 1.6 μm. By comparison, under the same conditions, a strong thermal conductivity reduction of ~50% is observed for BAs, indicating that long MFP phonons contribute substantially more to heat conduction in BAs crystals. Our measurements (Fig. 3B) are consistent with the DFT-predicted results for these materials (*8*, *16*, *18*). Phonons with long phonon MFPs (1 to 10 μm) contribute to a very high portion of BAs's total thermal conductivity (>50%). By comparison, in most known materials, phonon MFPs are distributed over a wider range (1 nm to 100 μm). Thus, we demonstrated that the ultrahigh thermal conductivity of BAs originates from the enhanced MFPs resulting from its distinctive phonon band structure.

We experimentally observed an ultrahigh thermal conductivity of 1300 W/m·K at room temperature in synthetic high-quality single-crystal BAs. Our study verifies the prediction from ab initio theory and establishes BAs as a benchmark material with the highest isotropic thermal conductivity of bulk metals and semiconductors. Our temperature-dependent data suggest that, unlike most common materials, high-order phonon anharmonicity strongly affects heat conduction in BAs. Furthermore, the phonon spectral contribution to thermal conductivity, investigated by exploiting the ballistic thermal transport, shows that compared to most materials, in BAs long phonon MFPs contribute to a substantially higher portion of the thermal conductivity. The investigation of fundamental transport mechanisms represents an important breakthrough in advancing the experiment-theory synergy for the rational design of new materials. Looking to the future, the ultrahigh thermal conductivity of BAs, together with its semiconducting nature and manufacturing integration, could revolutionize the current technological paradigms of thermal management and possibly extend the roadmap for high-power electronics.

REFERENCES AND NOTES

1. M. M. Waldrop, *Nature* **530**, 144–147 (2016).
2. P. Ball, *Nature* **492**, 174–176 (2012).
3. S. Chu, A. Majumdar, *Nature* **488**, 294–303 (2012).
4. W. L. Arman Shehabi, Sarah Smith, Dale Sartor, Richard Brown, Magnus Herrlin, Jonathan Koomey, Eric Masanet, Nathaniel Horner, Inês Azevedo, United States Data Center Energy Usage Report (2016); https://ses.lbl.gov/publications/united-states-data-center-energy.
5. International Technology Roadmap for Semiconductors, ITRS 2.0 2015 Edition; www.itrs2.net/.
6. J. M. Ziman, *Electrons and Phonons: The Theory of Transport Phenomena in Solids. Oxford Classic Texts in the Physical Sciences* (Oxford Univ. Press, 1960).
7. G. A. Slack, *J. Phys. Chem. Solids* **34**, 321–335 (1973).
8. L. Lindsay, D. A. Broido, T. L. Reinecke, *Phys. Rev. Lett.* **111**, 025901 (2013).
9. N. Mingo, D. A. Broido, *Phys. Rev. Lett.* **93**, 246106 (2004).
10. N. Mingo, D. A. Broido, *Phys. Rev. Lett.* **95**, 096105 (2005).
11. A. Ward, D. A. Broido, D. A. Stewart, G. Deinzer, *Phys. Rev. B* **80**, 125203 (2009).
12. K. Esfarjani, G. Chen, H. T. Stokes, *Phys. Rev. B* **84**, 85204 (2011).
13. L. Lindsay, D. A. Broido, T. L. Reinecke, *Phys. Rev. Lett.* **109**, 095901 (2012).
14. M. N. Luckyanova *et al.*, *Science* **338**, 936–939 (2012).
15. Y. Hu, L. Zeng, A. J. Minnich, M. S. Dresselhaus, G. Chen, *Nat. Nanotechnol.* **10**, 701–706 (2015).
16. T. Feng, L. Lindsay, X. Ruan, *Phys. Rev. B* **96**, 161201 (2017).
17. C. Uher, *Physics (College Park Md.)* **6**, 76 (2013).
18. D. A. Broido, L. Lindsay, T. L. Reinecke, *Phys. Rev. B* **88**, 214303 (2013).
19. R. M. Wentzcovitch, M. L. Cohen, P. K. Lam, *Phys. Rev. B Condens. Matter* **36**, 6058–6068 (1987).
20. M. Lax, P. Hu, V. Narayanamurti, *Phys. Rev. B* **23**, 3095–3097 (1981).
21. L. Lindsay, D. A. Broido, T. L. Reinecke, *Phys. Rev. B* **88**, 144306 (2013).
22. S. Tamura, *Phys. Rev. B* **30**, 849–854 (1984).
23. J. A. Perri, S. Laplaca, B. Post, *Acta Crystallogr.* **11**, 310 (1958).
24. F. V. Williams, R. A. Ruehrwein, *J. Am. Chem. Soc.* **82**, 1330–1332 (1960).
25. J. Osugi, K. Shimizu, Y. Tanaka, *Proc. Jpn. Acad.* **42**, 48 (1966).
26. S. M. Ku, *J. Electrochem. Soc.* **113**, 813 (1966).
27. A. F. Armington, *J. Cryst. Growth* **1**, 47–48 (1967).
28. T. L. Chu, A. E. Hyslop, *J. Appl. Phys.* **43**, 276–279 (1972).
29. P. Rudolph, Ed., *Handbook of Crystal Growth, Vol. II, Bulk Crystal Growth* (Elsevier, 2015); http://store.elsevier.com/Handbook-of-Crystal-Growth/isbn-9780444633033/).
30. B. Lv *et al.*, *Appl. Phys. Lett.* **106**, 074105 (2015).
31. F. Tian *et al.*, *Appl. Phys. Lett.* **112**, 031903 (2018).
32. N. H. Protik, J. Carrete, N. A. Katcho, N. Mingo, D. Broido, *Phys. Rev. B* **94**, 045207 (2016).
33. B. E. Warren, *X-ray Diffraction* (Addison-Wesley, MA, 1969).
34. Materials and methods are available as supplementary materials.
35. D. B. Williams, C. B. Carter, *Transmission Electron Microscopy: A Textbook for Materials Science* (Springer, Boston, MA, 2009).
36. J. S. Kang, H. Wu, Y. Hu, *Nano Lett.* **17**, 7507–7514 (2017).
37. D. G. Onn, A. Witek, Y. Z. Qiu, T. R. Anthony, W. F. Banholzer, *Phys. Rev. Lett.* **68**, 2806–2809 (1992).
38. L. Wei, P. K. Kuo, R. L. Thomas, T. R. Anthony, W. F. Banholzer, *Phys. Rev. Lett.* **70**, 3764–3767 (1993).
39. J. R. Olson *et al.*, *Phys. Rev. B Condens. Matter* **47**, 14850–14856 (1993).
40. A. Maradudin, A. Fein, *Phys. Rev.* **128**, 2589–2608 (1962).
41. L. Lindsay, D. A. Broido, *J. Phys. Condens. Matter* **20**, 165209 (2008).
42. F. Yang, C. Dames, *Phys. Rev. B* **87**, 035437 (2013).

ACKNOWLEDGMENTS

We thank H. Albrecht for editorial help, T. Aoki from UCI Materials Research Institute for help with TEM study, and the support from UCLA CNSI and Nanolab. **Funding:** Y.H. acknowledges support from a CAREER award from the EPM and TTP programs of the National Science Foundation under grant 1753393, a Young Investigator Award from the United States Air Force Office of Scientific Research under grant FA9550-17-1-0149, a PRF Doctoral New Investigator Award from the American Chemical Society under grant 58206-DNI5, the UCLA Sustainable LA Grand Challenge, and the Anthony and Jeanne Pritzker Family Foundation. **Author contributions:** Y.H. proposed and directed the research. Y.H. and J.S.K. designed the experiment; J.S.K., M.L., and H.N. performed the experiment; H.W. performed the ab initio calculations. All authors discussed the results and commented on the manuscript. **Competing interests:** The authors declare no competing financial interests. **Data and materials availability:** All data are available in the manuscript or the supplementary materials.

SUPPLEMENTARY MATERIALS

www.sciencemag.org/content/361/6402/575/suppl/DC1
Materials and Methods
Supplementary Text
Figs. S1 to S3
References (*43*–*58*)

12 March 2018; accepted 21 June 2018
Published online 5 July 2018
10.1126/science.aat5522